

Optimizing Proprotor Blades Using Coupled Aeroacoustic and Aerodynamic Sensitivities

R. Omur Icke¹, and Oktay Baysal²
Old Dominion University, Norfolk, VA, 23529, USA

Leonard Lopes³
NASA Langley Research Center, Hampton, VA, 23681, USA

Boris Diskin⁴
National Institute of Aerospace, Hampton, VA, 23666, USA

A quieter and aerodynamically more efficient proprotor design requires high-fidelity and well-integrated optimization and analysis tools. To fulfill that requirement, the present paper delivers a methodology based on multidisciplinary, adjoint-based, discrete optimization. SU2-based code development involves the implementation of aeroacoustic analysis, adjoint computations, and integrations into a multidisciplinary rotorcraft optimization suite. Submodules utilized in the optimization are verified with wind tunnel data to demonstrate the accuracy of aerodynamic and aeroacoustic analyses. The developed code is used for NASA's helically twisted proprotor to maximize the aeroacoustic performance of the proprotor while holding thrust constant. The optimization process considers multiple flight conditions (hence, multipoint), which are forward flight and hovering. As an outcome of the analyses, the optimized blade design propagates lower noise as perceived by multiple observers in both flight conditions.

I. Introduction

Urban Air Mobility (UAM) is one of the most popular proposed solutions for altering traffic problems in populated areas. In this context, the proposed types of vehicles mainly consist of rotors and propellers powered by electric motors. However, those rotary-wing components can contribute excessively to noise generation. Therefore, a significant noise concern emerges due to urban air vehicles in or around residential areas. Reducing noise emitted by air vehicles is critically important to improve public acceptance of such vehicles for operations in densely populated areas.

An accurate prediction of noise is a challenging task requiring a detailed representation of unsteady, turbulent flow fields, long distance propagation of the acoustic disturbances, and evaluation of complex and evolving noise metrics. An aircraft design process that includes optimization to minimize noise typically involves many design variables while adhering to aerodynamic performance constraints. The adjoint method enables gradient-based optimization of such problems, where the number of design variables far exceeds the number of design objectives. The computational cost of evaluating the adjoint-based sensitivities is independent of the number of design variables [1]. To date, significant progress has already been achieved by adjoint-based aerodynamic shape optimization for

¹ Corresponding Author. PhD Candidate, Mechanical & Aerospace Engineering, Member AIAA, ricke001@odu.edu.

² Professor & Eminent Scholar, Mechanical & Aerospace Engineering, Associate Fellow, AIAA, obaysal@odu.edu.

³ Senior Research Aerospace Engineer, Aeroacoustics Branch, MS 461, Leonard.V.Lopes@nasa.gov.

⁴ Research Fellow, Associate Fellow, AIAA, Boris.Diskin@nianet.org.

both steady and unsteady problems [1-5]. However, there are very few studies on acoustically optimized rotorcraft, and almost none that considers aerodynamics and aeroacoustics in the optimization formulation [6, 7].

A computational framework presented in a recent paper [8] was developed to analyze a complex flowfield generated by prop rotor and the associated acoustic wave propagation. The framework is based on the SU2-suite, which is an open-source collection of tools that solve the governing partial differential equations (PDEs) of fluid flow and PDE-constrained optimization problems on unstructured grids [9, 10]. Demonstrations of SU2-based aeroacoustic analysis for stationary sources have previously been reported [11]. The authors have now expanded this code to include a computational aeroacoustic (CAA) module using Farassat's Formulation 1A (F1A) [12]. This module offers an efficient approach to compute acoustic pressures at arbitrary observer locations, by performing boundary integrals once the required field data are provided. In this manner, the radiated noise can be calculated, given the near-field flow data supplied by a CFD solution. The aeroacoustic analysis module is validated by comparing with the predictions generated by NASA's aeroacoustics code, ANOPP2 [13], through an interface between SU2 and ANOPP2 for data transfer in both directions.

The first objective of the present paper is to show the confidence level of the SU2 suite to compute the aerodynamic and aeroacoustic performance of the prop rotor, by verifying with wind tunnel data. The second objective of the present paper is to construct an adjoint-based optimization framework that includes aeroacoustic and aerodynamic evaluation with multipoint assessments. Another goal is to use this multidisciplinary framework for shape optimization of the prop rotor blades. This problem is cast as a noise reduction optimization for two flight conditions, while adhering to a thrust constraint.

The present paper will demonstrate the developments of the framework by predicting the noise generated by a prop rotor in both forward flight and hover using Farassat's Formulation 1A (F1A) [12]. The aerodynamic analysis module is verified by comparing its results with available experimental data. The adjoint-based sensitivities are obtained by algorithmic differentiation and validated through comparison with complex-step sensitivities. As the design evolves through the optimization cycle, the described control points readjust the computational grid on the fly. Finally, comparisons of the aeroacoustic performance of the baseline and optimized designs are discussed.

II. Methodology

A. Optimization Framework

Before summarizing the steps of each of the modules, the overall methodology is presented graphically as a flowchart (Fig. 1). First, the aerodynamic and aeroacoustic analyses determine the values of the objective (or cost) function and the constraints on the baseline grid by using shape design variables, α . The optimizer, Scipy-SLSQP [14], a gradient-based optimization tool, requires gradients for projecting a search direction. It finds the descent direction, along with the objective function, by utilizing the line search approach. To eliminate the cost of the gradient computation, the optimizer does not recompute the gradients if existing gradients are sufficient to proceed with the line search. If gradients are required, the process solves the adjoint equations. Afterward, the tools acquire the derivatives of the objective function and the constraints with respect to the conserved variables. The system utilizes the derivatives and computes sensitivities with respect to the design variable.

The optimization cycle continues with the evaluation step that involves the objective function, the constraints, the side constraints (upper and lower bounds of design variables), the gradients, and the design vector. Then, another checkpoint controls the condition of convergence by computing the residual of the objective function. If the error is lower than the threshold value, the optimizer computes the new design variable vector, α^{new} . Otherwise, the optimization cycle ends. Next, the system sends the new variable vector to the section performing readjustment of the surface and volume grids. Finally, the updated grid is utilized for the computations at the following design steps, and the loop repeats.

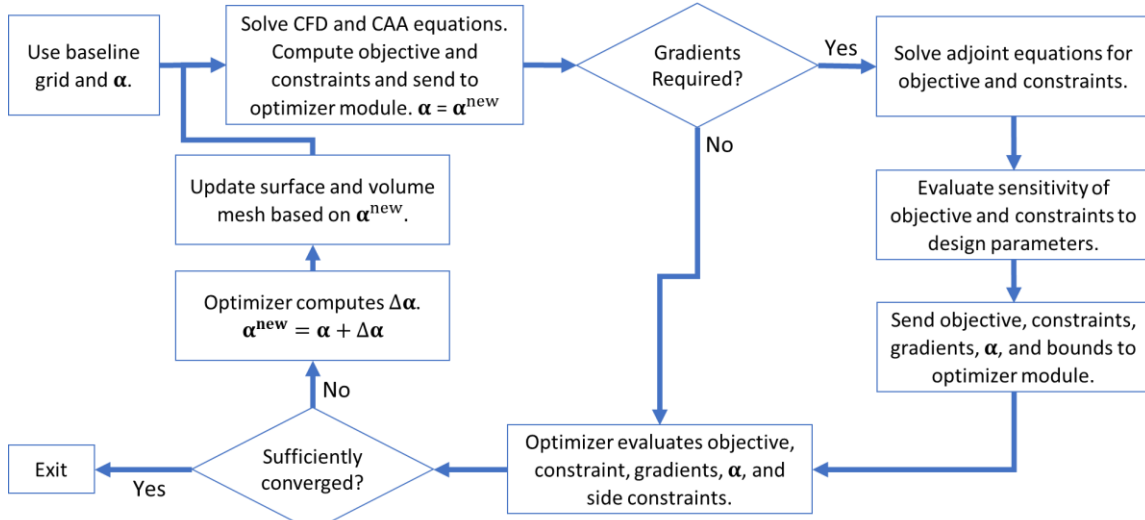


Figure 1: The gradient-based optimization cycle.

B. CFD Analysis for Noise Generation

The software SU2 solves the Unsteady Reynolds-averaged Navier-Stokes (URANS) equations to analyze compressible, turbulent flows commonly found in aerospace engineering problems. Throughout the simulations, an in-house developed code based on SU2-v7.1.1 is employed. The governing equations are spatially discretized using a finite volume method on unstructured grids. The time marching of the semidiscretized URANS equations is performed by a dual time-stepping method. The Spalart-Allmaras (SA) turbulence model is employed in the present study. Further details and references are cited in Ref. [8].

For the discretization of the flow equations, the Jameson-Schmidt-Turkel (JST) scheme is utilized with second and fourth-order dissipations and without any limiters. These configurations are based on the best practices reported in Ref. [15]. The Green-Gauss method is employed for the spatial gradients. The resulting linear systems are solved using the Flexible Generalized Minimum Residual (FGMRES) method and the Krylov preconditioner [16] with an error tolerance of $1E-6$.

The convergence criterion is five orders of magnitude reduction of the continuity residual at each inner time iteration. After 1,800-time steps, which corresponds to six prop rotor revolutions, the solution attains the limiting cycle, and provides a near-periodic state. The simulation continues for 3 additional revolutions of the prop rotor before the data for the acoustic predictions are extracted. These output data consist of the instantaneous node coordinates and the pressure values on the solid surfaces for each time step.

C. CAA Analysis of Noise Propagation

The scope of the present study is limited to predicting the tonal noise emitted from the prop rotor motion. Due to the required additional effort for the broadband noise, it is deferred to the future. Therefore, the implemented method, Farassat 1A formulation [12], only captures tonal noise. Farassat reported a family of integral formulations of the Ffowcs Williams and Hawkins (FWH) equation by assuming a free field Green's function. In the F1A formulation used herein, the quadrupole term is neglected; hence the pressure fluctuations at an observer location are the sum of the thickness and loading noise.

Previously, Zhou et al. have reported a similar approach [11] by utilizing a permeable surface limited to fixed sources in a so-called "wind tunnel configuration," where the source and observer move together in a stationary medium. In the present study, an impermeable surface approach is used with a source time dominant implementation. Moreover, the presently developed code can compute time-accurate noise sources using the more expanded version of F1A formulation that considers the time-accurate surface coordinates. Further details and references are cited in Ref. [8], where benchmark studies have been accomplished using ANOPP2's Farassat Formulation 1A Internal Functional Modules (AF1AIFM) [13].

Presented in Figure 2 is the time history of the acoustic pressure propagated by the tilt rotor XV-15 in forward flight. The microphone is located at 100 diameters away in the rotor plane. The aeroacoustic computations obtained

from two different software suites (SU2 vs. ANOPP2) demonstrate excellent agreement. SU2-CFD obtains the flow data in the respective formats needed by SU2-CAA and AF1AIFM codes.

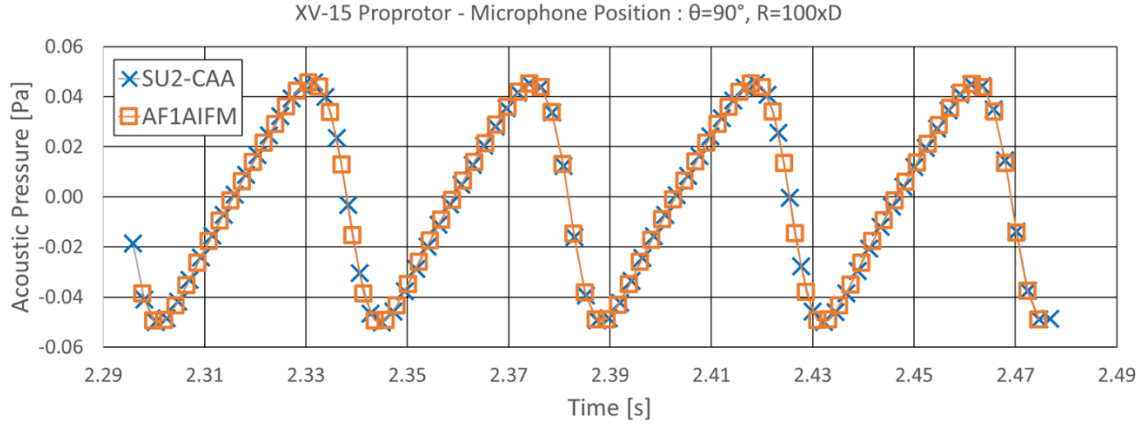


Figure 2: Acoustic pressure comparison of SU2-CAA and AF1AIFM for the microphone located at 100 diameters away in the rotor plane.

D. Sensitivities and Gradient-Based Optimization

A powerful feature of SU2 is the availability of algorithmic-differentiation (AD) rendered sensitivities by the utility CoDiPack [17]. By successive applications of the chain-rule differentiation through the SU2 code, both the flow analysis output and its derivative with respect to prescribed design variables are computed simultaneously. A remarkable feature of AD, owing to its construction, is that it does not incur any truncation errors, rendering derivatives that are at machine accuracy.

An optimization problem is defined to demonstrate the present methodology. The objective functional, J , is chosen as the overall sound metric; a function of the state variables, \mathbf{U} , and the grid coordinates, \mathbf{X} , which are, in turn, functions of the vector, $\boldsymbol{\alpha}$, of design variables. The discretized residual of the flow and acoustic equations, R , is introduced as a constraint function, which also is, in turn, a function of vectors \mathbf{U} and \mathbf{X} :

$$\underset{\boldsymbol{\alpha}}{\text{minimize}} \quad J(\mathbf{U}(\boldsymbol{\alpha}), \mathbf{X}(\boldsymbol{\alpha})) \quad (1)$$

$$\text{subject to} \quad R(\mathbf{U}(\boldsymbol{\alpha}), \mathbf{X}(\boldsymbol{\alpha})) = 0. \quad (2)$$

Next, this definition needs to be extended to be utilized for a problem with time-accurate noise surfaces. It must comply with the unsteady simulations, grid motions, and the CFD-CAA coupling. Previously, Zhou et al. [11] applied the adjoint-based discrete optimization for stationary surfaces, where they utilized dual time stepping. Albring et al. [18] showed how to implement the grid motion into the optimization problem. By compounding these two steps and extending for the problem at hand, a new optimization problem definition is introduced as follows:

$$\underset{\boldsymbol{\alpha}}{\text{minimize}} \quad J(\mathbf{U}^n, \mathbf{X}^n, \boldsymbol{\alpha}), \quad (3)$$

$$\text{subject to} \quad \mathbf{U}^n = \mathbf{G}^n(\mathbf{U}^n, \mathbf{U}^{n-1}, \mathbf{U}^{n-2}, \mathbf{X}^n, \mathbf{X}^{n-1}, \mathbf{X}^{n-2}), \quad (4)$$

$$\mathbf{X}^n = \mathbf{M}^n(\boldsymbol{\alpha}) \quad n = 1, \dots, N, \quad (5)$$

where \mathbf{M}^n denotes the grid readjustment equation and \mathbf{G}^n is an iteration of pseudotime stepping. The symbol n represents the time iteration index and the objective function, J , is evaluated for all n up to N . Next, the problem is recast as a Lagrangian (or penalty) function as follows:

$$L(\boldsymbol{\alpha}, \mathbf{U}^n, \mathbf{X}^n, \bar{\mathbf{U}}^n, \bar{\mathbf{X}}^n) = J(\mathbf{U}^n, \mathbf{X}^n, \bar{\mathbf{U}}^n, \bar{\mathbf{X}}^n, \boldsymbol{\alpha}) + \sum_{n=1}^N [(G^n(\mathbf{U}^n, \mathbf{U}^{n-1}, \mathbf{U}^{n-2}) - \mathbf{U}^n)^T \bar{\mathbf{U}}^n] + \sum_{n=1}^N [(\mathbf{M}^n(\boldsymbol{\alpha}) - \mathbf{X}^n)^T \bar{\mathbf{X}}^n]. \quad (6)$$

where \bar{U}^n and \bar{X}^n are flow and grid adjoint variables, respectively. By differentiating the Lagrangian function with respect to α , \bar{U}^n and \bar{X}^n , the first-order optimality conditions are obtained:

$$\frac{dL}{dU^n} = 0 = \frac{\partial J}{\partial U^n} - \bar{U}^n + \frac{\partial G^n}{\partial U^n} \bar{U}^n + \frac{\partial G^{n-1}}{\partial U^n} \bar{U}^{n-1} + \frac{\partial G^{n-2}}{\partial U^n} \bar{U}^{n-2}, \quad (7)$$

$$\frac{dL}{dX^n} = 0 = \frac{\partial J}{\partial X^n} + \frac{\partial G^n}{\partial X^n} \bar{U}^n + \frac{\partial G^{n-1}}{\partial X^n} \bar{U}^{n-1} + \frac{\partial G^{n-2}}{\partial X^n} \bar{U}^{n-2} - \bar{X}^n, \quad (8)$$

$$\frac{dL}{d\alpha} = \frac{dJ}{d\alpha} + \sum_{n=1}^N \left[\left(\frac{\partial M^n}{\partial \alpha} \right)^T \bar{X}^n \right]. \quad (9)$$

After rearranging Eqs. (7) and (8), the adjoints of the CFD and the grid equations become

$$\bar{U}^n = \frac{\partial J}{\partial U^n} + \frac{\partial G^n}{\partial U^n} \bar{U}^n + \frac{\partial G^{n-1}}{\partial U^n} \bar{U}^{n-1} + \frac{\partial G^{n-2}}{\partial U^n} \bar{U}^{n-2}, \quad (10)$$

$$\bar{X}^n = \frac{\partial J}{\partial X^n} + \frac{\partial G^n}{\partial X^n} \bar{U}^n + \frac{\partial G^{n-1}}{\partial X^n} \bar{U}^{n-1} + \frac{\partial G^{n-2}}{\partial X^n} \bar{U}^{n-2}, \quad (11)$$

and the general form of the sensitivity derivatives of the objective function Eq. (9) becomes

$$\frac{dJ}{d\alpha} = \frac{d}{d\alpha} M^T(\alpha) \frac{1}{N} \sum_{n=1}^N \bar{X}^n. \quad (12)$$

These equations are solved as presented in the flowchart below (Figure 3). The CFD solver outputs the state variables that are fed into the CAA solver and the adjoint computations. Subsequently, the CAA solver obtains the fluctuating component of pressure, p' , the objective function, J , its derivatives with respect to the grid, and the state variables for the surfaces, Γ_p . Next, the adjoint CFD solver computes the flow adjoints used as input for the computation of grid adjoints. Finally, the algorithmic differentiator calculates the sensitivities with respect to the design variable vector, α .

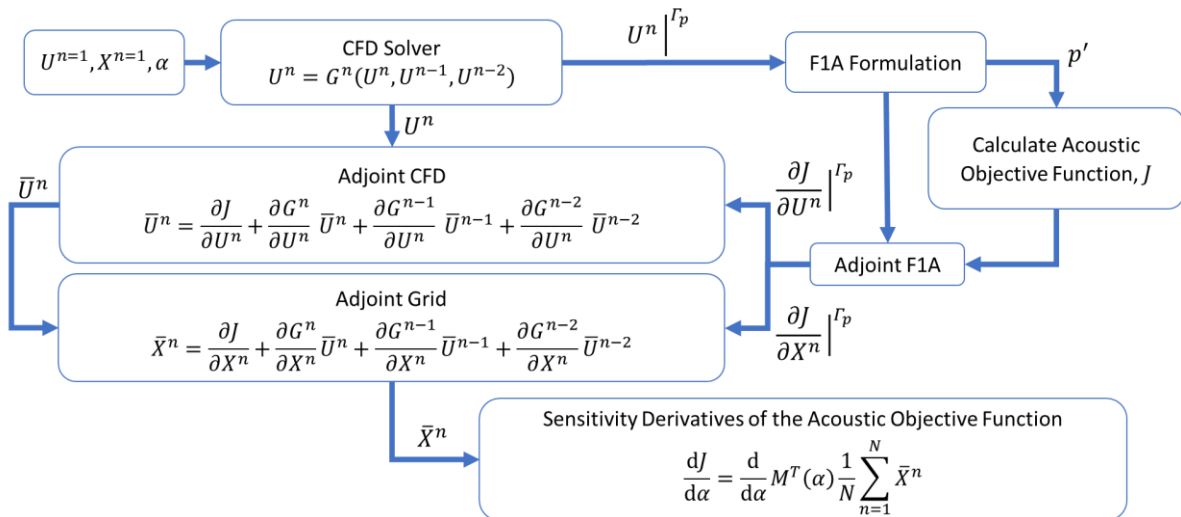


Figure 3: Flowchart of adjoint sensitivities for coupled aerodynamics and aeroacoustics.

III. Submodules

What follows are the subsections on aerodynamics and aeroacoustics, which are used in the optimization framework. Following them is the subsection on the adjoint sensitivities and their verification.

A. Aerodynamics

The first demonstration is to evaluate the noise from the three-bladed helically twisted prop rotor (3BHTR), which employs an exponential function of blade twist as a function of radius to achieve uniform inflow in hover. The 3BHTR in this study is a small-sized prop rotor having three blades, a hub, and a nacelle, as seen in Figure 4. The blade has a constant NACA 0012 airfoil profile from hub to tip, and it is twisted by utilizing the same chord length at each station. The chord length and the diameter of the prop rotor are 1.5 in and 24 in, respectively. The distribution of the twist angle is given by,

$$\phi\left(\frac{r}{R}\right) = \text{atan} \frac{P}{\pi D \cdot \frac{r}{R}}, \quad (13)$$

where ϕ is the twist angle function of nondimensional radius, r/R , and P is propeller pitch, equal to 16 in.

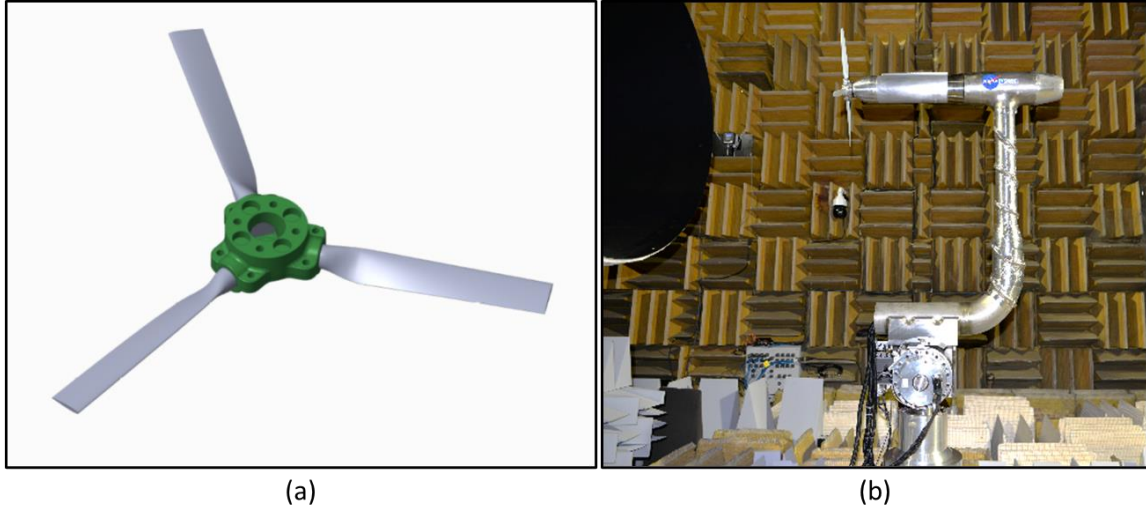


Figure 4: Three-bladed, helically twisted prop rotor (3BHTR): (a) CAD model and (b) wind tunnel model in LSAWT.

In the present work, the prop rotor is investigated under two different flight conditions. First, hover in a rotor configuration, where the freestream velocity equals zero. The rotational speed of the prop rotor is 7,200 RPM, yielding a tip Mach number of 0.666. When it is investigated in propeller configuration, that is, for the forward flight condition, the Mach number for the freestream velocity is 0.111. The rotational speed and the tip Mach number are also slightly different; they are 7,157 RPM and 0.668, respectively. Those flow conditions are based on the data collected from NASA's Low-Speed Aeroacoustic Wind Tunnel (LSAWT). Comparisons between the thrust and torque values predicted by SU2 and those measured in LSAWT are shown in Table 1. Considering the error values, the numerical results show high fidelity for the forward flight condition.

Figure 5 shows the instantaneous vorticity isosurfaces around blades for (a) propeller configuration (forward flight condition) and (b) rotor configuration (hover condition). Also, the skin friction distribution over the blades demonstrates qualitatively the pressure gradients on the surfaces. These visuals attest to the complexity of the flow in the wakes of the blades. Hover conditions involve complex flow regimes, including flow separations. While the skin friction around the tip region for the forward flight appears smoothly distributed (Fig. 4a), hover flight causes sharp skin friction gradients on the blade surfaces (Figure 5b). Therefore, the error margin between the wind tunnel

and CFD may be higher for the hovering proprotor (Table 1). Overall, these predictions from SU2 show satisfactory results to be utilized later in the optimization framework.

Table 1: Comparison of CFD and wind tunnel results for three-bladed helically twisted proprotor (3BHTP).

	Forward Flight			Hover		
	LSAWT	SU2-CFD	Error%	LSAWT	SU2-CFD	Error%
Thrust [N]	115.95	113.07	2.48	262.47	269.63	2.73
Torque [Nm]	8.16	8.14	0.36	16.55	14.86	10.24

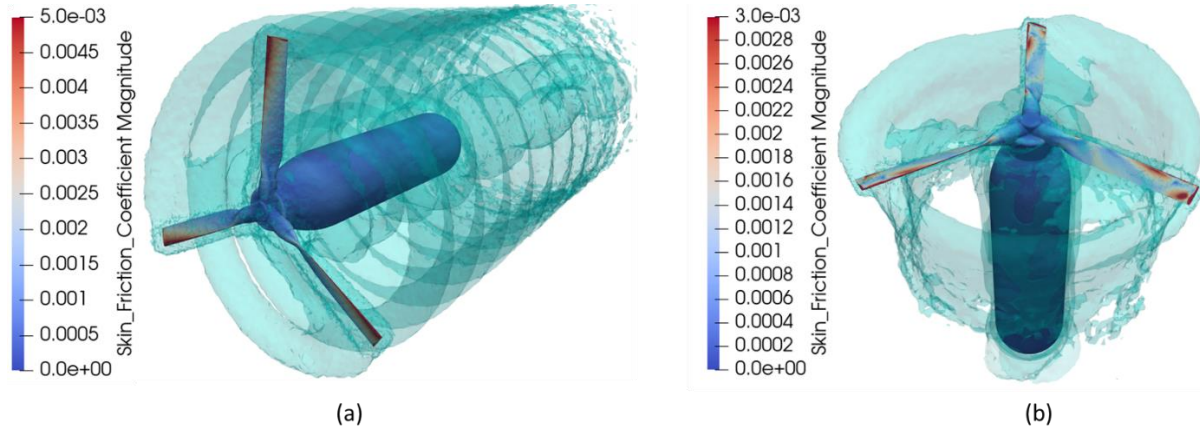


Figure 5: Instantaneous vorticity isosurfaces around proprotor and skin friction distribution over the blades: (a) propeller configuration with Q -criterion= 150 s^{-2} ; (b) rotor configuration with Q -criterion= 800 s^{-2} .

B. Aeroacoustics

As shown above in the flowcharts, after receiving data from the flow analysis, the CAA solver computes the acoustic propagation at prescribed observer locations. In Figure 6, the coordinate system is shown based on the origin point of the proprotor for the microphone position. R/D , θ , and φ represent the coordinates of the observer in 3-D space.

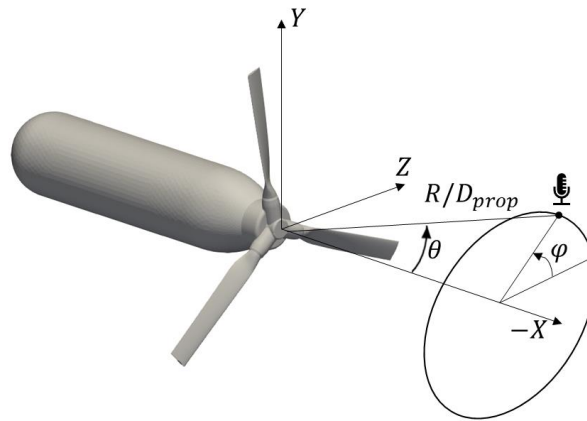


Figure 6: Coordinate system for microphone position.

As the first demonstration, an acoustic simulation is conducted for the proprotor in the forward flight case. Figs. 7 and 8 show the time history of acoustic pressure attained from SU2-CAA and LSAWT for a randomly selected pair of observers. Here, one observer is placed 10.5 proprotor diameters away with described θ and φ angles, which are set as 114.6 and 40, respectively. For the second observer, those numbers are 9.5, 94.6, and 40, respectively.

The obtained data show the noise propagation generated only by the propotor blades and hub. The predicted results and the wind tunnel results show reasonable agreement. Although not shown here, comparisons were made for many other observers, and the selected figures here are indicative of those comparisons.

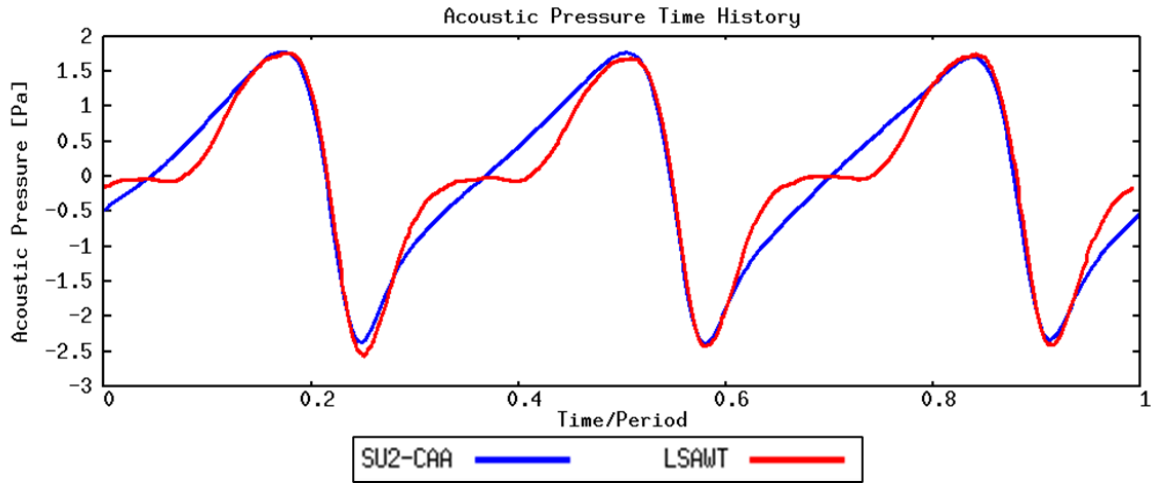


Figure 7: Time history of acoustic pressure for an observer, located at $R/D=10.5$, $\theta=114.6^\circ$, and $\phi=40^\circ$ (observer-14).

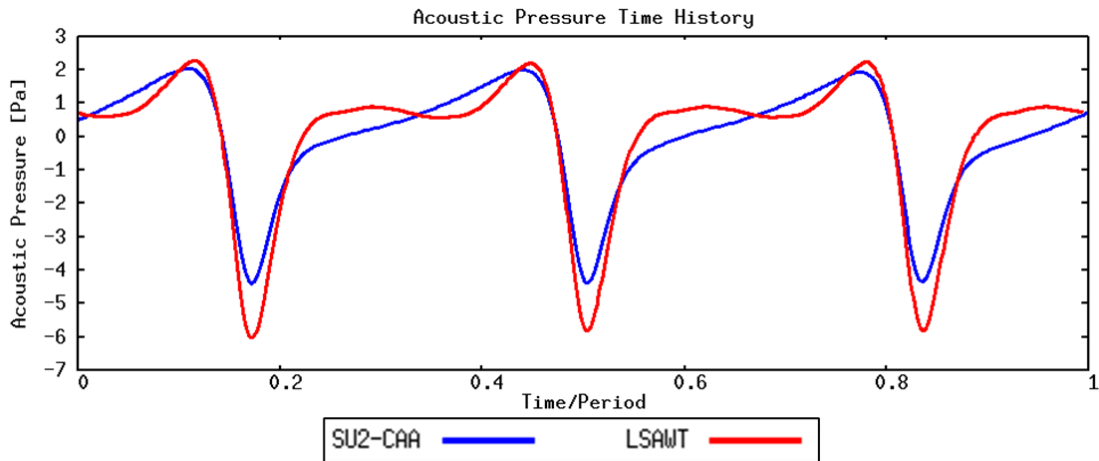


Figure 8: Time history of acoustic pressure for an observer, located at $R/D=9.5$, $\theta=94.6^\circ$, and $\phi=40^\circ$ (observer-10).

The present CAA tool can convert acoustic pressure data from the time domain to the frequency domain by utilizing a discrete Fourier transform. Thus, the sound pressure level (SPL) versus frequency data are obtained as described in Ref. [19]. For the SPL calculations, the reference pressure is taken as 2×10^{-5} Pa. The highest SPL value corresponds to the fundamental blade passage frequency (BPF), which is 360 Hz. In addition to the time domain comparison, the spectral comparison is performed to show the fidelity of predictions. The data in both the time and the frequency domains confirm that the simulations are close to the experimental data, and it is reasonable to continue this work with SU2-CAA predictions.

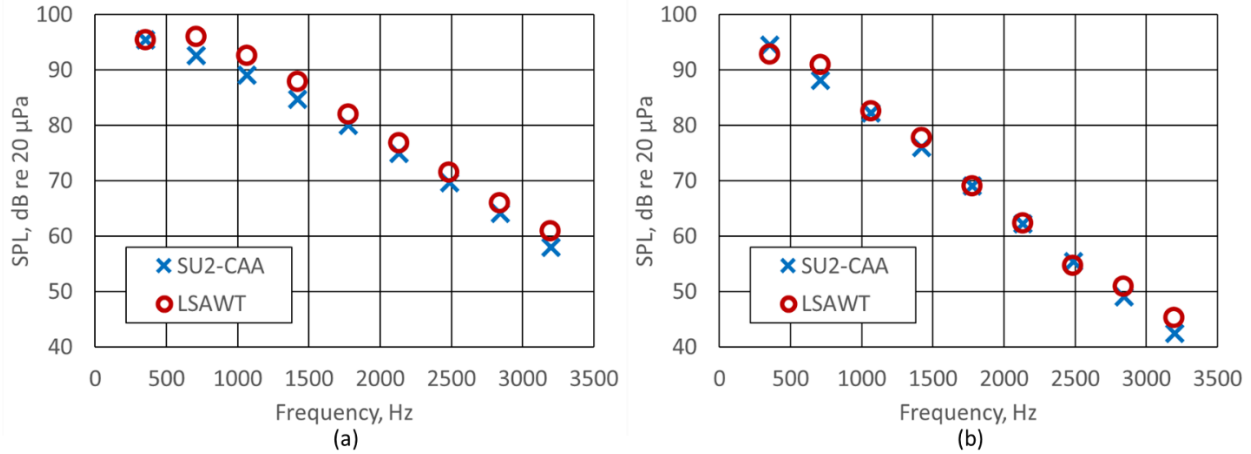


Figure 9: Spectral comparison of SU2-CAA predictions and LSAWT data for: (a) observer-10 and (b) observer-14.

The verification studies continue with investigating another comparison showing the sound pressure level (SPL) values perceived by a described microphone pattern. Herein, 27 microphones are positioned from upstream to the downstream region by keeping a constant distance in the y and z direction according to the propotor origin. Both in the CAA and wind tunnel tests, the same microphone patterns are utilized.

The design evaluation must involve a complete assessment of the aeroacoustic performance of the propeller and the rotor by using multiple observer points. Figure 10(a) and 10(b) show SPL values for different θ angles for forward flight and hover conditions, respectively. In the plots, SPLs corresponding to 3 different blade passage frequencies (BPF) is compared. The marked curves represent wind tunnel results, and the straight lines come from the CAA analyses. The results are quite satisfactory for both forward flight and hover for fundamental frequency (1xBPF). However, the graphs indicate that the prediction-based data have lower SPLs for the harmonics (2x and 3x BPF), particularly for the microphone located near the in-plane direction, the angles between 75° and 105° . That discrepancy may be the result of limitations in geometric accuracy, numerical methods, and the identified flow conditions. Overall, the CAA tool is verified by the wind tunnel test, and it has a high confidence level to be utilized in the optimization process.

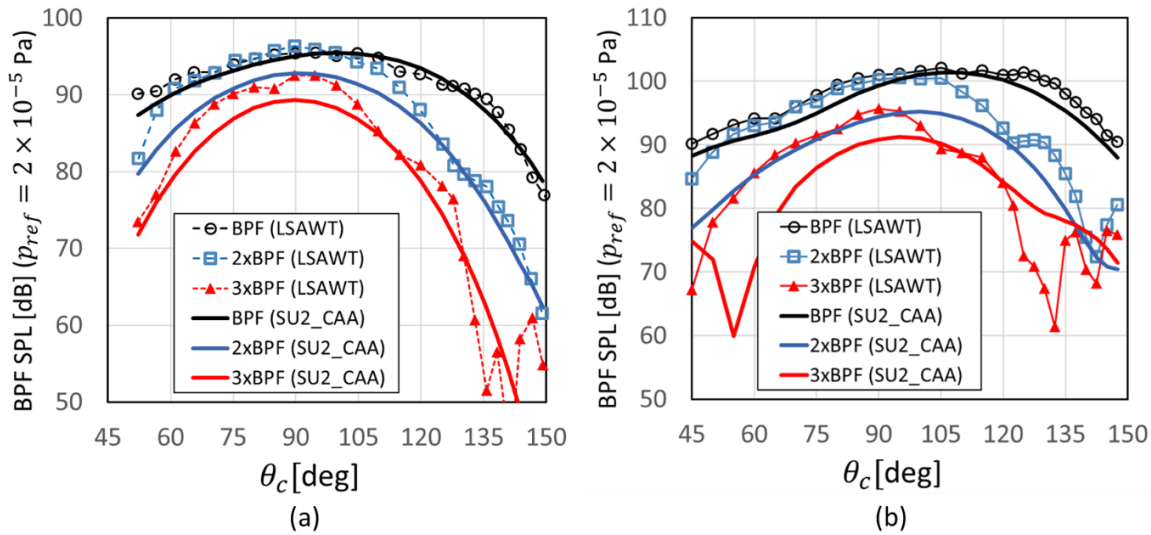


Figure 10: Sound pressure values corresponding to fundamental blade passage frequency versus observer locations at different θ angles (with constant $x/D_{prop} = 3.73$ and $y/D_{prop} = 4.45$) for: (a) forward flight, and (b) hover conditions.

C. Adjoint Sensitivities

Gradient values with respect to a specific variable, for example, the design parameters, can be efficiently calculated by solving the adjoint equation. In the present study, both the aerodynamic and aeroacoustic gradients are derived by the adjoint approach, then implemented in the algorithmic differentiation utility, CoDiPack [17].

The CoDiPack utility has previously been implemented in SU2 as a built-in function that can be called through the computational processes. First, the developed CAA code includes the adjoints stored for each variable within the panel on the surface and the sample loop. Through the acoustic computations, the recording of the dependencies continues until the determination of the objective function. Once the objective function is introduced, the algorithmic differentiation (AD) tool computes adjoints. Herein, the precision of the AD-based partial derivatives needs to be declared. To verify the accuracy of the gradients obtained by algorithmic differentiation, they are compared with gradients computed by complex differentiation (CD) [20],

$$F'(x_0) \approx \frac{\text{Im}(F(x_0 + ih))}{h}, \quad (14)$$

where the step value, h , is set to 10^{-50} for the perturbation. The implemented method includes computation for only one node on the blade surface. By the applied perturbation on the node, it is possible to find partial derivatives. The location of the node should be around the tip region that is more sensitive to noise propagation. For an illustrative purpose, let the function of the acoustic objective be shown as J that equals sound pressure level. The calculations, AD and CD, derive partial derivatives with respect to the conservative variables, as shown in Table 2. The results in Table 2 indicate relative errors in the order of 10^{-12} or smaller; hence, a successful verification has been achieved. (In the table below, the first nonmatching digits are printed in red.)

Table 2: Sensitivity verification of 3BHTP.

	Sensitivities with respect to grid coordinates		
	$\frac{\partial J}{\partial x}$	$\frac{\partial J}{\partial y}$	$\frac{\partial J}{\partial z}$
Complex	3.08076498355256E-06	4.34231946052742E-06	-4.69514172868562E-06
Algorithmic	3.08076498355797E-06	4.34231946052224E-06	-4.69514172868941E-06
Relative Error	1.76E-12	1.19E-12	8.07E-13
	Sensitivities with respect to conserved state variables		
	$\frac{\partial J}{\partial \rho}$	$\frac{\partial J}{\partial(\rho u_x)}$	$\frac{\partial J}{\partial(\rho u_y)}$
Complex	5.56754302938544E-05	8.14390936251084E-07	-1.57902880043867E-07
Algorithmic	5.56754302938265E-05	8.14390936251096E-07	-1.57902880043919E-07
Relative Error	5.01E-13	1.47E-14	3.29E-13
	$\frac{\partial J}{\partial(\rho u_z)}$	$\frac{\partial J}{\partial(\rho E)}$	
Complex	-1.44517576643667E-07	-3.24143151177512E-10	
Algorithmic	-1.44517576643658E-07	-3.24143151177473E-10	
Relative Error	6.23E-14	1.20E-13	

Additionally, sensitivities with respect to the grid coordinates are demonstrated in Figure 11. On a single blade surface, the distribution of the instantaneous partial derivatives gives an idea about sensitivities. As seen in that figure, the most sensitive nodes are located in the near-tip region. That situation gives an idea of how to set up the design variables in an optimization process. Briefly, the effective way to improve aeroacoustic performance is to modify the tip region.

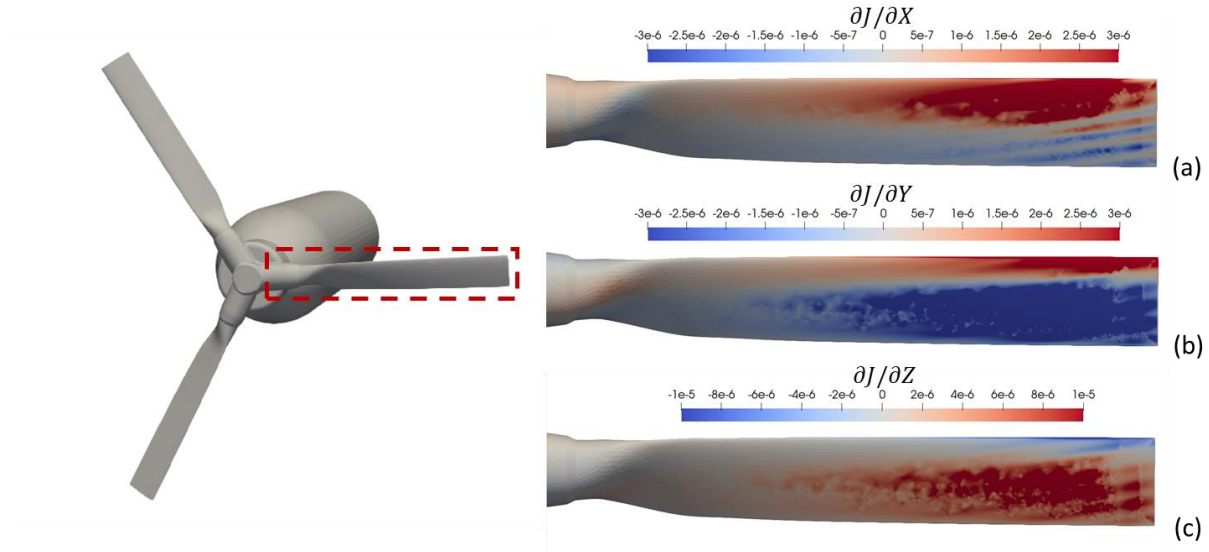


Figure 11: Sensitivities with respect to the grid coordinates; (a) $\partial J/\partial x$; (b) $\partial J/\partial y$; and (c) $\partial J/\partial z$ on the blade surface framed with red dashed line.

Table 3: Finite difference validation of the sensitivity for a design variable (movement of the tip inward direction).

	Forward Flight	
	Sound Pressure Level	Thrust
Finite Difference	1.2294903020E-02	-8.4799762120E-06
Adjoint	1.2883194023E-02	-8.4798234176E-06
Error	4.57E-02	1.80E-05
	Hover	
	Sound Pressure Level	Thrust
	3.6245346334E-02	-6.3438192941E-06
	3.6441611124E-02	-6.3358191756E-06
Error	5.39E-03	1.26E-03

Another verification study is conducted for the adjoints obtained for a particular variable. The variable controlling the blade tip deformation inward direction is preferred for that study. Gradients obtained from adjoint operation are mainly compared with the gradients attained from the finite difference method, as seen in Table 3. According to the error values, it can be stated that the gradients are similar. On the other hand, the adjoint has superior advantages in computational cost. Therefore, utilizing adjoint for the optimization is preferable to the finite difference method.

IV. Optimization

A. Parametrization

The scope of the present paper is the shape optimization of propeller blades. In the optimization loop, the blade shape needs to be updated before the next set of computations. SU2 has its own grid deformation tool, SU2-DEF,

that moves grid points while keeping the same connectivity. That enables the user to morph the grid but within a limited range to avoid negative volume structure. The grid deformation process employs the free form deformation (FFD) boxes. The control points at the box's corners manage the movement of the surface grid that the FFD box encloses.

The reconstruction of the FFD boxes for the 3BHTP is performed (Figure 12(a)). Roughly, FFD boxes wrap 80% of the span of each blade. The individual FFD box defined for each blade moves simultaneously. As depicted in Figure 12(b), the control points move and rotate in the direction shown with colored arrows. To prevent sharp changes on the surface, the control points at the near-hub station are set to be fixed.

The control points near trailing and leading edges move in the direction of red arrows to parametrize chord length. Moreover, middle control points move in the direction of the blue arrow to assess the cambered airfoil effects on the performance. Additionally, the tip region inward movement is controlled as shown with green arrows. That deformation changes the blade span and tip speed. Lastly, planes at each radial station manage the twist angle of airfoils by the given rotation inputs. Overall, optimization studies consist of 55 design variables using the Bezier-Bernstein polynomials for the deformations.

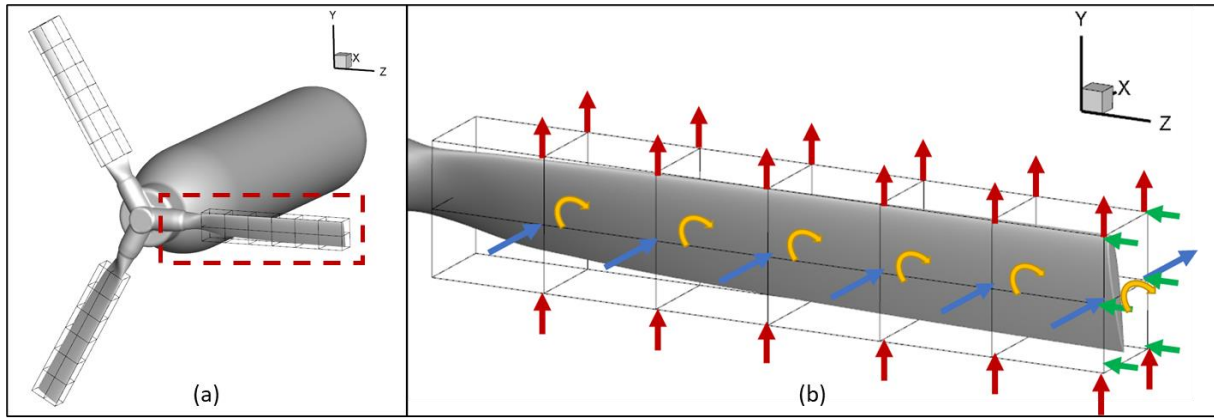


Figure 12: (a) FFD boxes wrapping three blades of the prop rotor and (b) parametrization of control points.

A multipoint optimization combines disparate flow regimes in one platform. To accomplish that, one objective function that rules all flow regions needs to be defined. Herein, an objective function corresponding to multiple observers and the multipoint-based optimization problem is described as follows:

$$F = 10 \log_{10} \left(\int_{\theta_{min,ff}}^{\theta_{max,ff}} \frac{\langle p^2 \rangle_{A,ff}}{\sin \theta} d\theta \right) + 10 \log_{10} \left(\int_{\theta_{min,h}}^{\theta_{max,h}} \frac{\langle p^2 \rangle_{A,h}}{\sin \theta} d\theta \right) - 20 \log_{10} \left(\frac{p_{ref}^2}{2\pi h^2} \right), \quad (15)$$

where F is the objective function and θ is the angle between the observer/microphone and the longitudinal axis of the prop rotor according to the center of the rotor. $\langle p^2 \rangle_{A,ff}$ and $\langle p^2 \rangle_{A,h}$ are A-weighted summations of all frequency data for the forward flight and hover conditions, respectively.

Furthermore, the constraint function also needs to be defined to include multipoint optimization. Throughout the processes, thrust is the only constraint in the optimization. The multipoint constraint function for the thrust is the summation of the thrust output derived from the CFD analysis for the hover and forward flight cases.

B. Results

The results obtained from the optimization are discussed in this section. First, a comparison of the optimum and baseline blade shapes is shown in Figure 13. The dashed black line and solid red line represent optimized and baseline surfaces, respectively. The optimized surface improves the aeroacoustic performance of the prop rotor in both forward flight and hovering while maintaining the thrust value. According to the comparison of airfoils at the different radial stations, chord length becomes shorter at the blade tip with a cambered profile. While the twist angle increases around the tip region, the middle sections have reduced twist angles.

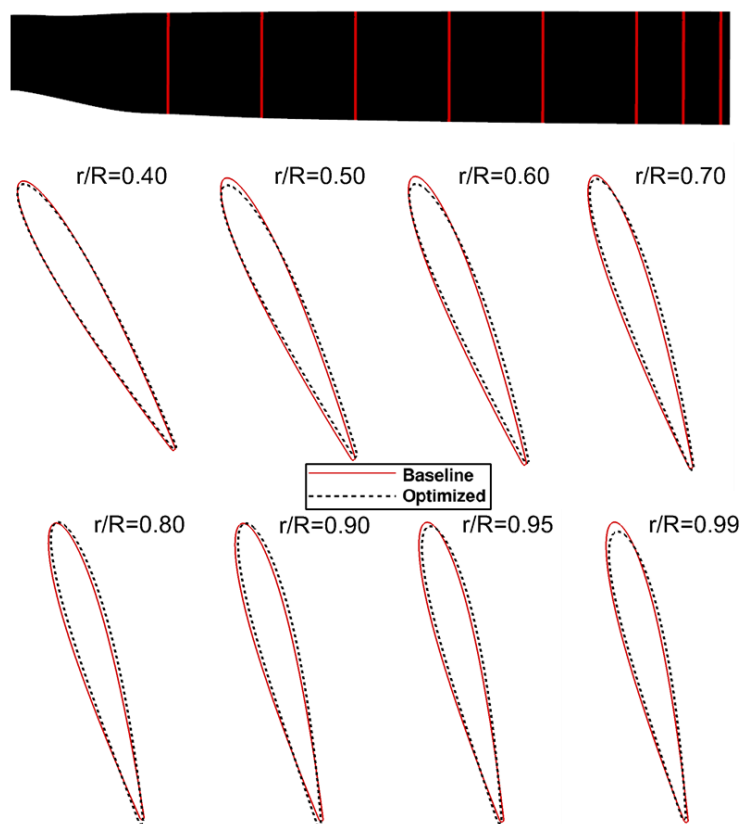


Figure 13: Radial sections of baseline and optimized blade geometries.

In addition, deformations at the tip include morphing in the radial direction. The optimization results indicate that the leading edge of the tip section moves inward, as seen in Figure 14. On the other hand, the trailing edge moves outward. That situation is due to the multidisciplinary objective where decreasing the blade radius increases the thickness noise, however, it reduces the thrust value. Therefore, the overall blade radius could not change.

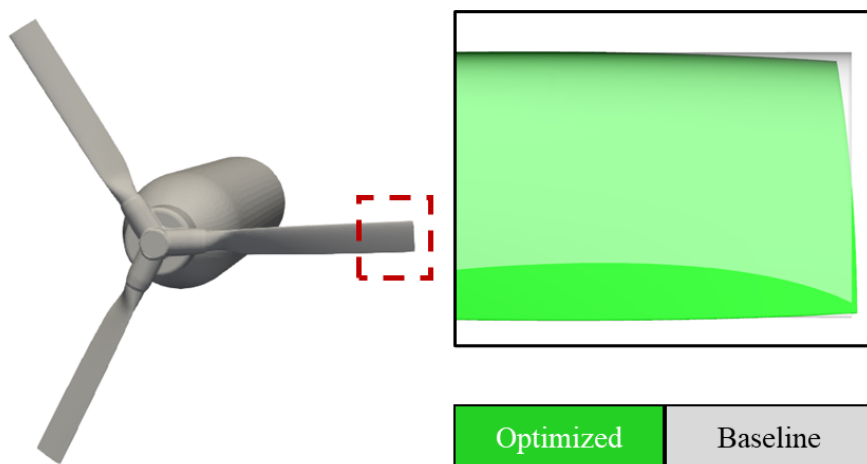


Figure 14: Blade deformation at the tip region.

The performance comparison of the blade shapes is evaluated from the aeroacoustic point of view. In Figure 15, SPL data corresponding to the blade passing frequency demonstrate the improvements in the noise levels for all observer points. The green lines represent the acoustic computation obtained from the optimized surface, and black lines are derived from the baseline surface. It is observed that the enhancements increase in the downstream region in comparison with the upstream region. As a result, the optimized surface offers quite satisfactory aeroacoustic performance for both hover and forward flight scenarios for all microphone positions.

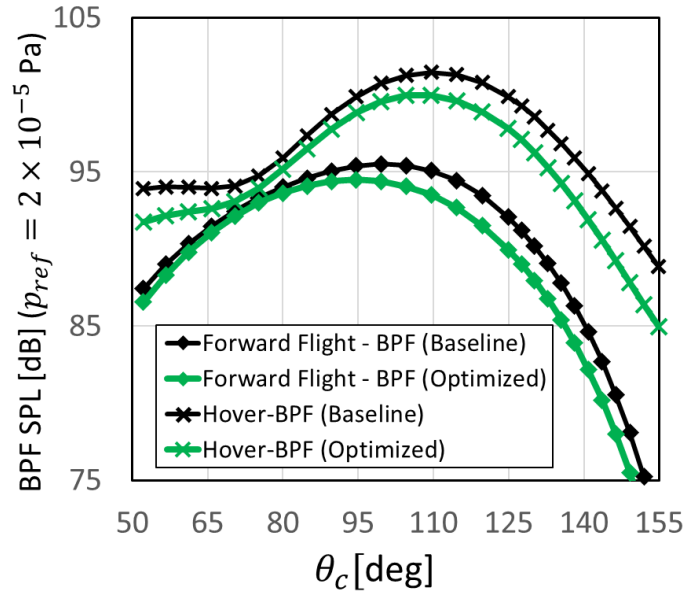


Figure 15: Comparison for SPL of baseline and optimized proprotor for the forward flight and hover cases.

Figure 16 demonstrates the comparison of baseline and optimized surfaces for the second and third harmonics. The results for the forward flight configuration (Figure 16(a)), are slightly different for all microphone positions. However, optimized design impacts the second and third harmonics considerably in hover configuration (Figure 16(b)).

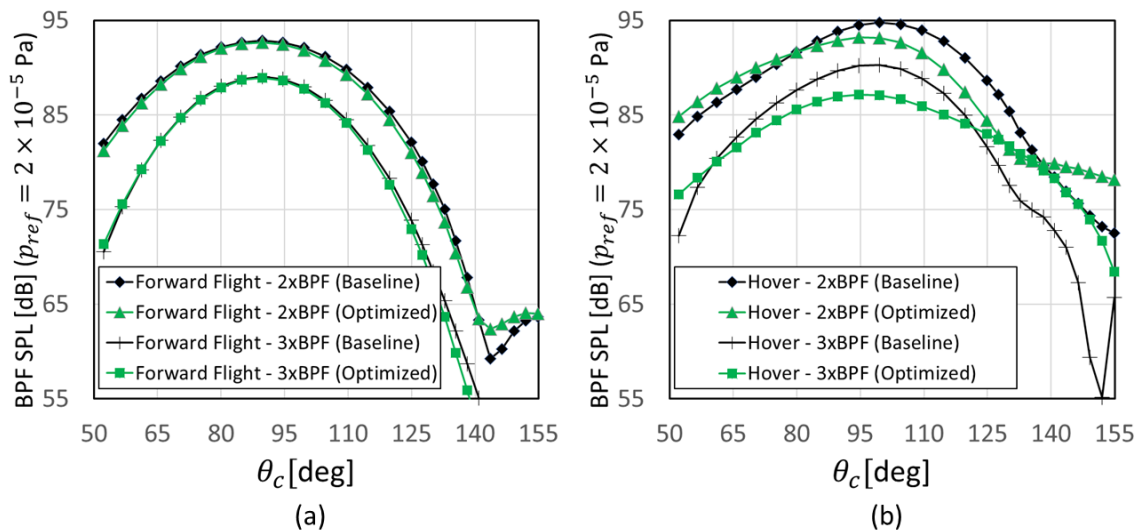


Figure 16: Comparison for SPL corresponding to the second and third harmonics of baseline and optimized proprotor for: (a) the forward flight, (b) hover configurations.

The aeroacoustic performance comparisons are also made for individual observer points. Figure 17 and Figure 18 show comparisons of the optimized and baseline results for θ angle equal to 94.6° and 114.6° , respectively. The time histories of acoustic pressure in Figure 17(a) and Figure 18(a) clearly demonstrate the improvements in the results derived by optimized surfaces. Improvement also can be seen on spectral data shown in Figs. Figure 17(b) and Figure 18(b). The performance difference between the two propellers primarily appear in the blade passing frequency, which is 360 Hz.

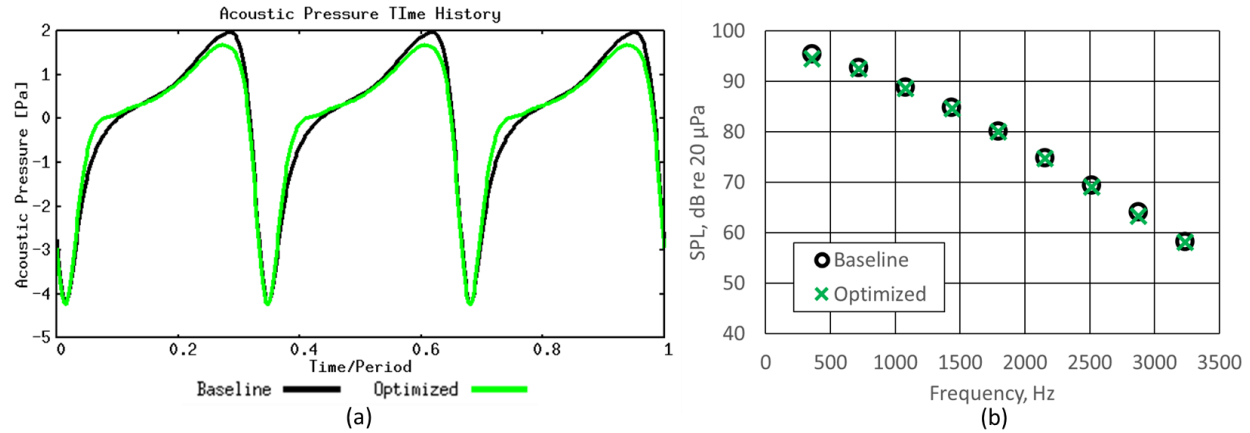


Figure 17: Comparison of the baseline and optimized surface for observer-10 ($\theta = 94.6^\circ$) in (a) time domain and (b) frequency domain.

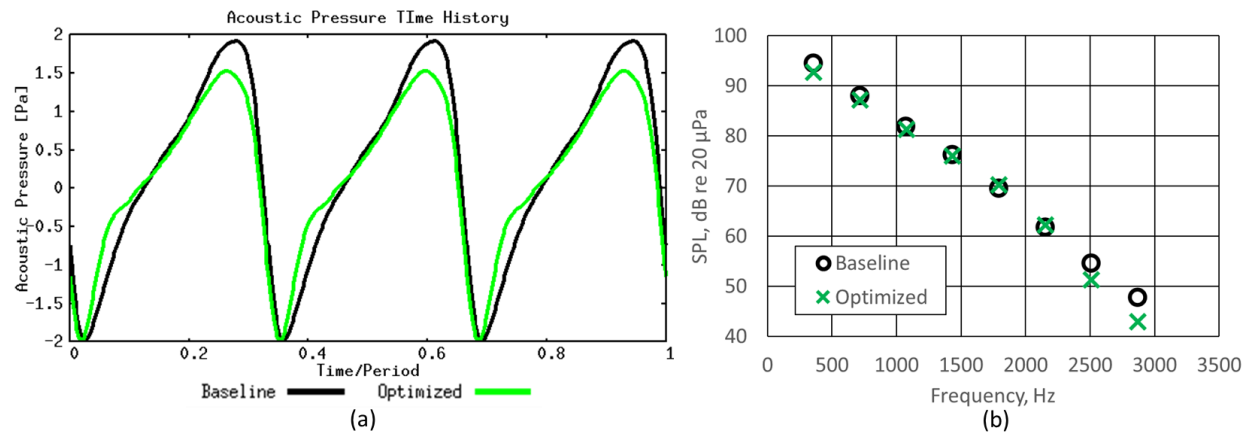


Figure 18: Comparison of the baseline and optimized surface for observer-14 ($\theta = 114.6^\circ$) in (a) time domain and (b) frequency domain.

Displaying the components of the acoustic pressure, which are thickness noise and loading noise, demonstrates which noise source is dominant or improved (Fig. 19). Comparing the optimized and the baseline surfaces helps us understand the improvements. Both Figure 19(a) and 19(b) indicate that the improvements originate from loading. On the other hand, thickness noise components are almost the same for both surfaces. Thickness noise is proportional to the tip speed. Therefore, the thickness noise is not expected to change much since the optimized blade is about the same span length as the baseline surface.

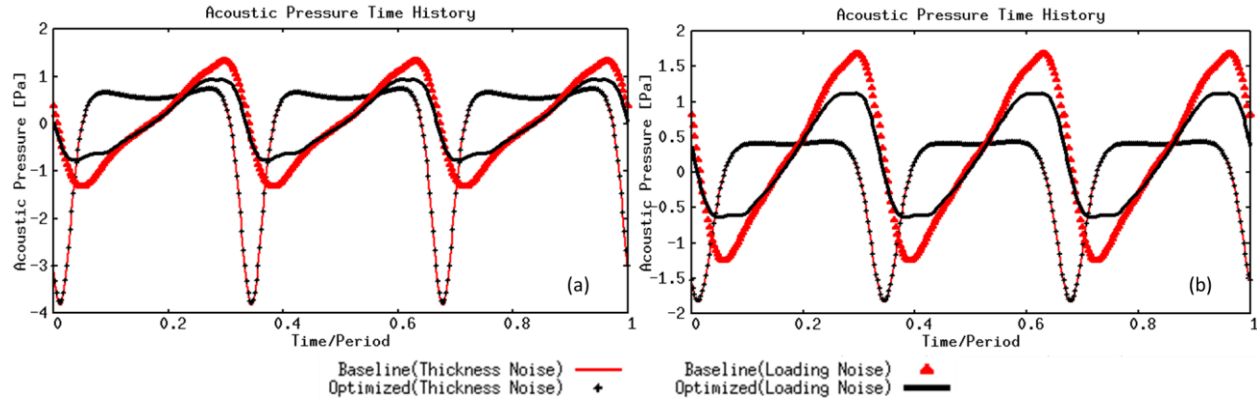


Figure 19: Thickness noise and loading noise components of the acoustic pressure emitted from baseline and optimized surfaces for: (a) observer-10, (b) observer-14.

V. Conclusions

A code is developed to demonstrate the overall multidisciplinary optimization methodology for aerodynamic and aeroacoustic performance of rotorcraft. When applied for a prop rotor, it successfully obtains a new blade shape that improves the aeroacoustic performance of the prop rotor and does not sacrifice the thrust. Besides, the present high-fidelity code demonstrates its accuracy, with its output being very close to wind tunnel results. This is accomplished by using the developed tool that accepts a *multidisciplinary* objective, conducts *multi-point* optimization, using *multiple* observers.

In future work, some of the limitations will be lifted, such as allowing more extensive grid deformation and much reduced computational times with more efficient integrations and schemes. Implementing a 3rd-party grid generator into the optimization cycle may help deform the grid freely while keeping the same grid quality. That enables the user to open the side constraints, resulting in a larger design space. Thus, the optimization tool will be able to achieve more aggressive shape deformation and more enhancements. Although the present results are obtained on single zone grids that rotate together with the whole domain, it will be valuable to implement the multizonal grid to simulate and optimize rotary and stationary wings in the same fluid domain.

Acknowledgments

This study is supported by a NASA Langley Research Center grant through the National Institute of Aerospace. The authors acknowledge the computer resources provided by the HPC of Old Dominion University, and Nikolas Zawodny of the Aeroacoustics Branch at NASA Langley for providing acoustic test data.

References

1. Baysal, O., and Ghayour, K. "Continuous Adjoint Sensitivities for Optimization with General Cost Functionals on Unstructured Meshes," *AIAA Journal* Vol. 39, No. 1, 2001, pp. 48-55.
doi: 10.2514/2.1269
2. Baysal, O., and Elshaky, M. E. "Aerodynamic design optimization using sensitivity analysis and computational fluid dynamics," *AIAA Journal* Vol. 30, No. 3, 1992, pp. 718-725.
doi: 10.2514/3.10977
3. Elshaky, M. E., and Baysal, O. "Shape Optimizing Nacelle near Flat-Plate Wing Using Multiblock Sensitivity Analysis," *Journal of Aircraft* Vol. 35, No. 1, 1998, pp. 33-38.
doi: 10.2514/2.2286
4. Wang, L., Diskin, B., Biedron, R. T., Nielsen, E. J., and Bauchau, O. A. "High-Fidelity Multidisciplinary Sensitivity Analysis and Design Optimization for Rotorcraft Applications," *AIAA Journal* Vol. 57, No. 8, 2019, pp. 3117-3131.
doi: 10.2514/1.J056587

5. Rumpfkeil, M., and Zingg, D. "Unsteady Optimization Using a Discrete Adjoint Approach Applied to Aeroacoustic Shape Design," *46th AIAA Aerospace Sciences Meeting and Exhibit, AIAA 2018-18*. American Institute of Aeronautics and Astronautics, 2008.
6. Fabiano, E., Mavriplis, D. J., and Sitaraman, J. "Adjoint - based Aeroacoustic Design Optimization for Blade Vortex Interaction Noise," *56th AIAA/ASCE/AHS/ASC Structures, Structural Dynamics, and Materials Conference, AIAA 2015-1801*. American Institute of Aeronautics and Astronautics, 2015.
7. Fabiano, E., Mishra, A., Mavriplis, D. J., and Mani, K. "Time-dependent Aero-acoustic Adjoint-based Shape Optimization of Helicopter Rotors in Forward Flight," *57th AIAA/ASCE/AHS/ASC Structures, Structural Dynamics, and Materials Conference, AIAA 2016-1910*. American Institute of Aeronautics and Astronautics, 2016.
8. Icke, R. O., Baysal, O., Lopes, L. V., Zhou, B. Y., Diskin, B., and Moy, A. "Toward Adjoint-Based Aeroacoustic Optimization for Propeller and Rotorcraft Applications," *AIAA Aviation 2020 Forum, AIAA 2020-3140*. American Institute of Aeronautics and Astronautics, 2020.
9. Economon, T. D., Palacios, F., Copeland, S. R., Lukaczyk, T. W., and Alonso, J. J. "SU2: An Open-Source Suite for Multiphysics Simulation and Design," *AIAA Journal* Vol. 54, No. 3, 2015, pp. 828-846. doi: 10.2514/1.J053813
10. Economon, T. D., Palacios, F., and Alonso, J. J. "An Unsteady Continuous Adjoint Approach for Aerodynamic Design on Dynamic Meshes," *15th AIAA/ISSMO Multidisciplinary Analysis and Optimization Conference, AIAA 2014-2300*. American Institute of Aeronautics and Astronautics, 2014.
11. Zhou, B. Y., Albring, T. A., Gauger, N. R., Economon, T. D., and Alonso, J. J. "An Efficient Unsteady Aerodynamic and Aeroacoustic Design Framework Using Discrete Adjoint," *17th AIAA/ISSMO Multidisciplinary Analysis and Optimization Conference, AIAA 2016-3369*. American Institute of Aeronautics and Astronautics, 2016.
12. Farassat, F. "Derivation of Formulations 1 and 1A of Farassat," *NASA/TM-2007-214853*. NASA Langley Research Center, 2007.
13. Lopes, L., and Burley, C. "ANOPP2 User's Manual: Version 1.2," *NASA/TM-2016-219342*. NASA Langley Research Center, Hampton, Virginia, 2016.
14. Kraft, D. "Algorithm 733: TOMP—Fortran modules for optimal control calculations," *ACM Trans. Math. Softw.* Vol. 20, No. 3, 1994, pp. 262–281. doi: 10.1145/192115.192124
15. Gomes, P., Economon, T. D., and Palacios, R. "Sustainable High-Performance Optimizations in SU2," *AIAA Scitech 2021 Forum, AIAA 2021-0855*. American Institute of Aeronautics and Astronautics, 2021.
16. Saad, Y. "A Flexible Inner-Outer Preconditioned GMRES Algorithm," *SIAM Journal on Scientific Computing* Vol. 14, No. 2, 1993, pp. 461-469. doi: 10.1137/0914028
17. Sagebaum, M., Albring, T., and Gauger, N. "High-Performance Derivative Computations using CoDiPack," *arXiv.org*, 2017.
18. Albring, T. A., Sagebaum, M., and Gauger, N. R. "Efficient Aerodynamic Design using the Discrete Adjoint Method in SU2," *17th AIAA/ISSMO Multidisciplinary Analysis and Optimization Conference, AIAA 2016-3518*. American Institute of Aeronautics and Astronautics, 2016.
19. Lopes, L. V., Iyer, V. R., and Born, J. "Robust Acoustic Objective Functions and Sensitivities in Adjoint-Based Design Optimizations," *55th AIAA Aerospace Sciences Meeting, AIAA 2017-1673*. American Institute of Aeronautics and Astronautics, 2017.
20. Martins, J. R. R. A., Sturdza, P., and Alonso, J. J. "The complex-step derivative approximation," *ACM Trans. Math. Softw.* Vol. 29, No. 3, 2003, pp. 245–262. doi: 10.1145/838250.838251